

ADHESIVES

Stereomicrostructure-regulated biodegradable adhesives

Zhen Zhang^{1†‡}, Ethan C. Quinn^{1†}, Jacob K. Kenny^{2,3}, Alexandra Grigoropoulos⁴, Jason S. DesVeaux^{2,3}, Tiffany Chen^{5,6,7}, Li Zhou¹, Ting Xu^{4,5,6,7*}, Gregg T. Beckham^{2,3*}, Eugene Y.-X. Chen^{1*}

Commercial adhesives are petroleum-based thermoset networks or nonbiodegradable thermoplastic hot melts, making them ideal targets for replacement by biodegradable alternatives. Poly(3-hydroxybutyrate) (P3HB) is a biorenewable and biodegradable alternative to conventional plastics, but microbial P3HB, which has a stereoperfect stereomicrostructure, exhibits no adhesion. In this study, by elucidating the fundamental relationship between chemocatalytically engineered P3HB stereomicrostructures and adhesion properties, we found that biodegradable syndio-rich P3HB exhibits high adhesion strength and outperforms common commercial adhesives, whereas syndiotactic, isotactic, or iso-rich P3HB shows no measurable adhesion. The syndio-rich stereomicrostructure brings about desired thermomechanical and viscoelastic properties of P3HB that enable strong adhesion to a range of substrates tested, including aluminum, steel, glass, and wood, and its performance is insensitive to molar mass and reprocessing or reuse.

Adhesives that bond between and seal surfaces have found widespread applications in various areas associated with daily life, including personal devices, electronics, automotive vehicles, construction, and packaging (1). Over the past decades, adhesives have witnessed continuous advances that impart high performance, durability, scalability, and affordability, approximating to a market share of more than US\$50 billion (2). However, despite their ubiquity, the end-of-life management and sustainability of adhesives are often overlooked. This oversight represents an important issue in the context of addressing the plastic waste crisis (3–6) and moving toward polymer sustainability (7–10), as nearly all adhesives on the market are petroleum-derived and nonbiodegradable (1, 11), including two major categories of commercial adhesives or glues: thermoset (cross-linked) networks, such as Gorilla Glue and J-B Weld, and thermoplastic hot melts, such as poly(ethylene-co-vinyl acetate) (EVA) (Fig. 1, A and B). In contrast to the commodity plastics used for packaging, which can be collected and recycled to some extent, recapturing disposed adhesives is often made difficult by their strong bonds with other materials.

To mitigate waste from plastic adhesives, recent efforts have been devoted to the development of more sustainable alternatives (12, 13). For example, a biobased adhesive was recently developed using epoxidized soy oil, malic acid, and tannic acid; upon cross-linking the epoxy and carboxylic acid groups at elevated temperature, adhesion strength comparable to that of current industrial products on sandblasted substrates was achieved (14). To address the end-of-life issue of adhesives, lignin-based (15) and polysaccharide-based (16) adhesives, some of which are potentially biodegradable, have been developed, typically to target wood substrates, and the adhesion strength can be largely affected by external factors, such as humidity, incorporated metal salts, and chemical modifications (16). Biodegradable polyester-based adhesives showed only limited adhesion strength (<2 MPa) on various substrates, even with optimization of the (co)polymer composition and the introduced additives (17, 18).

Poly(3-hydroxybutyrate) (P3HB), the most prominent member of the large poly(3-hydroxyalkanoate) (PHA) family, is a natural, microbially produced polyester that is biodegradable in managed (industrial composting) or unmanaged conditions (fresh water, sea water, and soil) (19), and it thus has long been considered a promising sustainable alternative to petroleum-based and/or nonbiodegradable plastics (20–24). The whole PHA family was rarely explored for its adhesion properties, because of the poor adhesion performance of medium-chain-length PHA (17), the brittleness of the biological P3HB that prevents adhesive behavior (25), and the lack of stereomicrostructural diversities and thereby a tunable viscoelasticity for microbial P3HB. This limitation has motivated recent advances in the chemocatalytic pathway to stereomicrostructurally diverse P3HB materials (Fig. 1C) (20, 25–28). In particular, syndio-rich P3HB

(*sr*-P3HB) was shown to be semicrystalline yet ductile and to exhibit biodegradation rates in fresh water and soil comparable to those of the microbial P3HB (26).

We hypothesized that understanding the relationship between stereomicrostructure and the adhesion property of P3HB could lead to P3HB materials with tunable adhesion strength. The basis for this hypothesis is threefold. (i) P3HB contains in-chain polar ester groups and hydroxyl chain ends that are essential adhesive moieties capable of forming strong physical interactions with various surfaces (29, 30). (ii) P3HB also has a polypropylene-like structural motif in the repeating unit that governs the thermomechanical and viscoelastic properties of the polymer through the stereochemistry of the backbone chiral carbon and thus can modulate adhesion strength of materials (Fig. 1C). (iii) Network formation is essential for energy dissipation, but most current high-performance adhesive materials rely on chemical cross-links that inherently limit their recyclability and degradability. We envisioned that rationally programming P3HB crystalline and amorphous domains, enabled by stereomicrostructural engineering, to form physically cross-linked networks in P3HB would enhance adhesion strength.

Stereomicrostructure effects on thermomechanical properties, chain configuration, and conformation

To test our hypothesis that P3HB could be engineered to exhibit adhesive properties, we first generated a library of P3HB stereomicrostructures. By understanding the interplay of molecular symmetry and steric matching between monomer and catalyst molecules (fig. S1, 1 to 10), we synthesized P3HB with the entire range of possible tacticities (Figs. 1C and 2A and table S1) using the catalyzed stereoselective ring-opening polymerization (ROP) of bioderived eight-membered racemic and meso-dimethyl diolides, *rac*- and *meso*-8DL^{Me}. For consistency, when comparing adhesion strength, we used a syndiotactic racemo triad [*rr*] value to denote a specific P3HB stereomicrostructure throughout: P3HB_[*rr*], where [*rr*] stands for the percentage of [*rr*] triads (which were found to be the most important factor determining the P3HB adhesion property). The diolide (8DL^{Me}) platform provided an ideal starting point for this investigation, owing to its ability to completely exclude a stereomicrostructure triad when desired (26). For example, when *rac*-8DL^{Me} is polymerized, [*rr*] triads cannot be produced, and when the same is applied to *meso*-8DL^{Me}, isotactic meso triads [*mm*] cannot be produced. We were able to synthetically engineer P3HB spanning the entire range of stereomicrostructures on the basis of the diastereomeric monomer and stereoselective catalyst choice. These include syndiotactic (*st*) and *sr*-P3HB abundant

¹Department of Chemistry, Colorado State University, Fort Collins, CO, USA. ²Renewable Resources and Enabling Sciences Center, National Renewable Energy Laboratory, Golden, CO, USA. ³BOTTLE Consortium, Golden, CO, USA.

⁴Department of Materials Science and Engineering, University of California, Berkeley, Berkeley, CA, USA.

⁵Department of Chemistry, University of California, Berkeley, Berkeley, CA, USA. ⁶Materials Science Division, Lawrence Berkeley National Laboratory, Berkeley, CA, USA. ⁷Kavli Energy NanoScience Institute, Berkeley, CA, USA.

*Corresponding author. Email: tingxu@berkeley.edu (T.X.); gregg.beckham@nrel.gov (G.T.B.); eugene.chen@colostate.edu (E.Y.-X.C.)

†These authors contributed equally to this work.

‡Present address: South China Advanced Institute for Soft Matter Science and Technology, School of Emergent Soft Matter, South China University of Technology, Guangzhou, China.

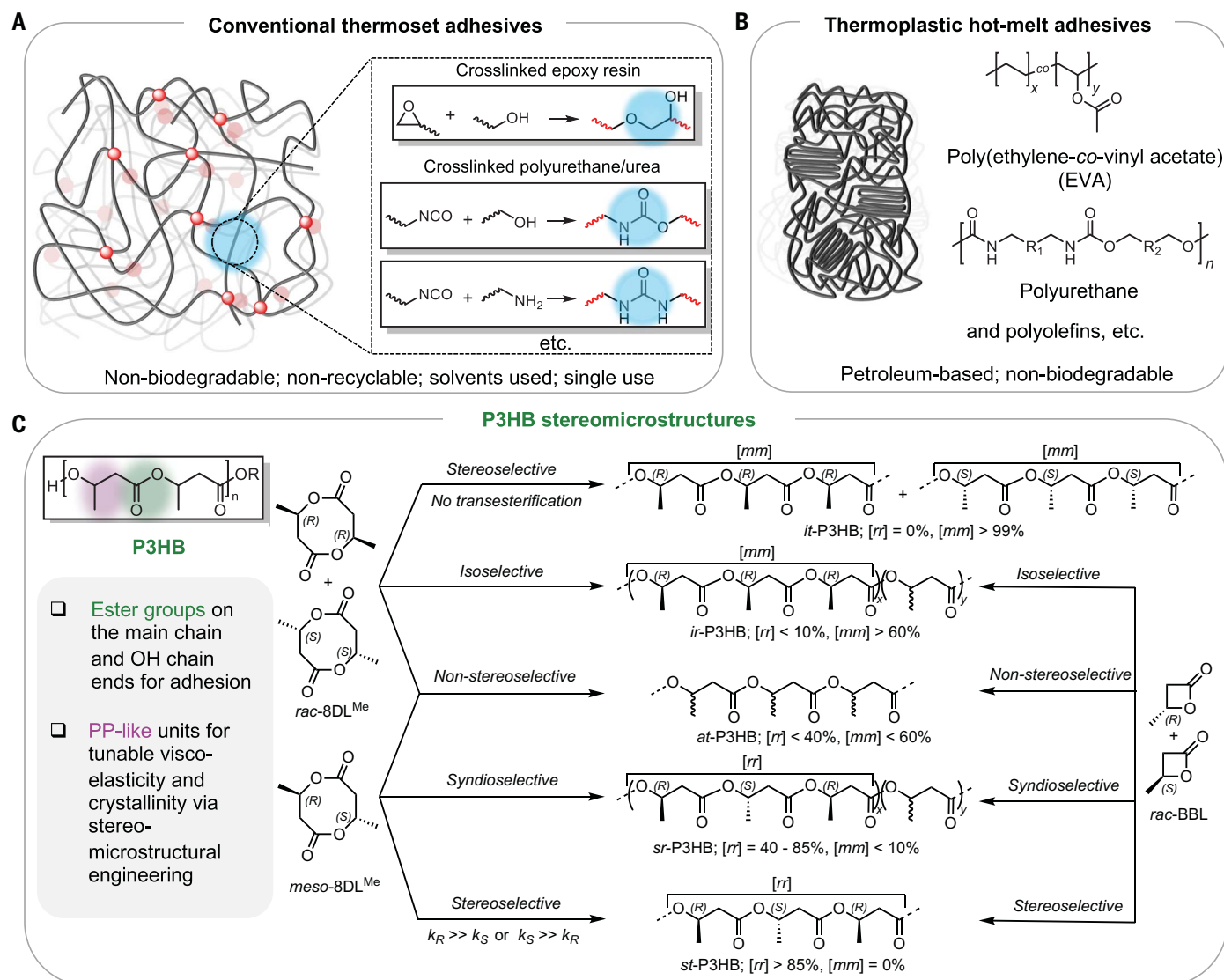


Fig. 1. Representative commercial adhesives and P3HB stereomicrostructures investigated in this study. (A) A generic cross-linked network structure illustrating conventional thermoset adhesives and representative cross-linking structural motifs. (B) A generic semicrystalline polymer structure illustrating conventional thermoplastic hot-melt adhesives and representative polymers including EVA.

(C) Synthetically engineered P3HB stereomicrostructures produced by catalyzed, stereoselective ROP for the study of the relationship between stereomicrostructure and adhesion property. k_R , rate constant for ring-opening at the acyl-oxygen bond adjacent to the *R* stereogenic center; k_S , rate constant for ring-opening at the acyl-oxygen bond adjacent to the *S* stereogenic center.

in $[rr]$ and $[mr]$ triads but devoid of $[mm]$ triads; isotactic (*it*) and iso-rich (*ir*)-P3HB abundant in $[mm]$ and $[mr]$ triads but devoid of $[rr]$ triads; and atactic (*at*)-P3HB having all triads. These P3HB materials were produced at moderate to high molar masses ($M_n = 38$ to 201 kDa) with low dispersities ($D = 1.01$ to 1.47). Because of the absence of chain-shuttling or epimerization with the diolide system (28), we were able to synthesize P3HB with designer stereomicrostructures. These include *it*-P3HB_[0] and *ir*-P3HB_[0] devoid of $[rr]$ triads and rich in $[mm]$ triads ($[mm] = 80$ to $>99\%$), and a range of *sr*-P3HB_[42-84] devoid of $[mm]$ triads and rich in $[rr]$ triads (42 to 84%). For comparative studies, we also synthesized *ir*-, *at*-, and *sr*-P3HB from *rac*- β -butyrolactone (*rac*-BBL) (table S2), where

the polymerization is less stereochemically controlled and thus offers a limited range of triads.

We analyzed the P3HB thermomechanical properties that are directly correlated to their adhesive performance and subsequent application demonstration. Specifically, we measured their melting-transition temperature (T_m) and percent crystallinity (x_c), as T_m gives a processing temperature for the adhesive application and the crystallinity dictates the viscoelastic behavior of the material, which further affects the adhesion behavior. In general, a moderate level of crystallinity is required for thermoplastics to be adhesive, whereas a high level of crystallinity will not allow for strong adhesion, as a proper portion of amorphous domains offering the viscous character is necessary for close contact

between the polymer and the substrates (30). As anticipated, with an increase in the highly crystallizable $[rr]$ triads, the T_m increased from 97.3°C to 168.8°C (figs. S6 to S10), and x_c increased from 22% to 56% accordingly (table S1). As a reference, *ir*-P3HB_[0] has a T_m of 108.8°C (table S1, entry 5). Regardless of the relative $[rr]$ triad variations, *sr*-P3HB_[rr] displays a similar thermal degradation temperature (T_d , defined as the temperature at 5% weight loss) of ~245°C (figs. S11 to S13), which is consistent with that of the reported P3HB (28). The difference in the P3HB stereomicrostructures has a substantial impact on their mechanical properties, as shown in Fig. 2B and figs. S14 to S16. With a highly stereoregular polymer backbone, both *it*-P3HB_[0] and *sr*-P3HB_[84] are strong (ultimate tensile stress

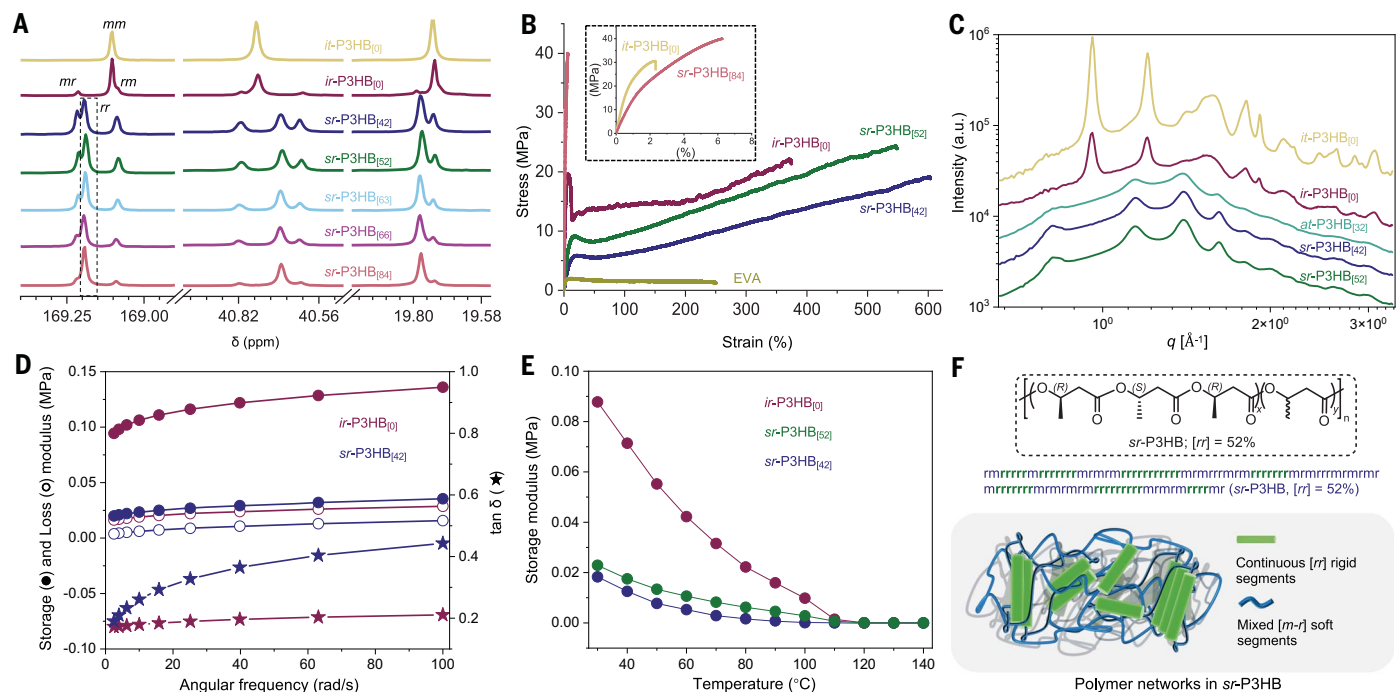


Fig. 2. Characterization of designer P3HB with diverse stereomicrostructures. (A) ^{13}C $\{^1\text{H}\}$ nuclear magnetic resonance spectra (CDCl_3) of P3HB in the carbonyl [169.00 to 169.25 parts per million (ppm)], methylene (40.56 to 40.82 ppm), and methyl (19.58 to 19.80 ppm) regions. The carbonyl resonance peaks were assigned to $[rm]$, $[mm]$, $[rr]$, and $[mr]$ triads as shown. (B) Stress-strain curves of *it*- and *ir*-P3HB $_{[0]}$, *sr*-P3HB $_{[84]}$, *sr*-P3HB $_{[52]}$, *sr*-P3HB $_{[42]}$, and EVA (from a glue stick). *ir*-P3HB $_{[0]}$ = entry 5, table S1. Strain rate = 5 mm min^{-1} , ambient

condition. The end point of each curve is the break point. (C) WAXS profiles of *it*-, *ir*-, *at*-, and *sr*-P3HB powder. *ir*-P3HB = entry 6, table S1. a.u., arbitrary units. (D) Storage modulus, loss modulus, and $\tan \delta$ for *sr*-P3HB $_{[42]}$ and *ir*-P3HB $_{[0]}$ (measured at 30°C). *ir*-P3HB $_{[0]}$ = entry 6, table S1. (E) Storage modulus for *sr*-P3HB $_{[42]}$, *sr*-P3HB $_{[52]}$, and *ir*-P3HB $_{[0]}$ at temperatures from 30° to 140°C (1 rad/s). *ir*-P3HB $_{[0]}$ = entry 6, table S1. (F) Sequence simulation of the *sr*-P3HB $_{[52]}$ backbone and illustration of the polymeric networks in *sr*-P3HB.

$\sigma_B = 28.6 \pm 3.0$ and 39.0 ± 3.9 MPa), hard (tensile modulus $E = 3.7 \pm 0.2$ and 1.6 ± 0.1 GPa), and brittle (elongation at break $\epsilon_B = 2.2 \pm 0.2$ and $6.1 \pm 1.4\%$). The P3HB with a reduced stereoregularity, such as *sr*-P3HB $_{[42]}$, *sr*-P3HB $_{[52]}$, and *ir*-P3HB $_{[0]}$, became softer ($E = 69.0 \pm 1.2$, 144.3 ± 6.8 , and 810.0 ± 28.5 MPa), ductile ($\epsilon_B = 595.7 \pm 46.8$, 553.3 ± 38.4 , and $354.3 \pm 54.9\%$), and tough (toughness $U_T = 66.7 \pm 7.9$, 89.5 ± 10.4 , and 55.7 ± 10.3 MJ m^{-3}). In comparison, the tensile properties of an EVA hot melt were much inferior, indicating a weak ($\sigma_B = 1.4 \pm 0.1$ MPa) and soft ($E = 131.3 \pm 13.3$ MPa) material (Fig. 2B and fig. S17).

Third, to gain a better understanding of the polymer microstructures, wide-angle x-ray scattering (WAXS) of the P3HB powders was performed to probe the polymer microstructures in the solid state (Fig. 2C). Consistent with the structure of *it*-P3HB (31, 32), both *sr*- and *ir*-P3HB showed an orthorhombic crystal structure. *ir*-P3HB $_{[0]}$ exhibited a scattering profile identical to that of *it*-P3HB $_{[0]}$ except for a lower peak intensity owing to the reduced crystallinity. For *sr*-P3HB $_{[42,52]}$, smaller crystal structure peaks with a large full width at half maximum were observed (fig. S27), indicating reduced and smeared crystalline regions relative to that of *ir*-P3HB $_{[0]}$, which is reminiscent of the drastically lowered modulus (< 0.1 GPa) and yield

stress (6.0 MPa) of *sr*-P3HB $_{[42]}$ compared with *ir*-P3HB $_{[0]}$ (~ 0.8 GPa and 19.8 MPa, respectively) and could potentially benefit close contact with the substrate during the adhesion test discussed below. This observation also validated that stereomicrostructural engineering can effectively balance the formation of nanoscopic hard domains in P3HB, that is, the crystalline region and the amorphous domain, to simultaneously tune the hardness and toughness of the materials while maintaining the reversibility of the cross-linkers. To probe the chain configuration, small-angle x-ray scattering (SAXS) was performed on *ir*- and *sr*-P3HB with various molar masses and tacticities in tetrahydrofuran solutions (10 mg ml^{-1}) (fig. S18). The scattering profiles were fitted with the Guinier-Porod model and the radius of gyration (R_g) of the corresponding P3HB was extracted (figs. S19 to S24). For *sr*-P3HB $_{[42]}$ with M_n ranging from 14 to 201 kDa, the dimension of the chain increases almost linearly with M_n as opposed to a certain scaling law for a Gaussian coil, suggesting a rodlike conformation of the continuous $[rr]$ segment that increases in its quantities with the increase of M_n and is responsible for rigidifying the polymer chain (fig. S25). In comparison, *sr*-P3HB $_{[52]}$, with a higher percentage of $[rr]$ triads in the backbone, was found to have a larger R_g (18.6 nm), likely because of longer continuous $[rr]$ seg-

ments in the polymer chain. Consistently, *ir*-P3HB $_{[0]}$ with a similar molar mass to *sr*-P3HB $_{[52]}$ (103 kDa versus 138 kDa) and devoid of any continuous $[rr]$ segments that are accountable for chain rigidification, displayed a much smaller R_g value of 11.8 nm (fig. S25).

Fourth, as the viscoelastic properties are closely connected to adhesive properties, we performed frequency sweeps on *sr*-P3HB $_{[42,52]}$ as well as *ir*-P3HB $_{[0]}$ at temperatures from 30° to 140°C (figs. S42 to S44) and then compared their viscoelastic properties. We found that *ir*-P3HB $_{[0]}$ has a smaller $\tan \delta$ (the ratio between viscous and elastic contributions of the modulus; Fig. 2D) and a much higher storage modulus than *sr*-P3HB $_{[42,52]}$ at the temperature range of 30° to 100°C (Fig. 2E). These findings suggest that *ir*-P3HB $_{[0]}$ lacks a sufficiently viscous character and is a much stiffer material compared with *sr*-P3HB $_{[42,52]}$, which would lead to nonideal contact with the substrates and thus low adhesion performance.

Lastly, to reveal effects of the stereomicrostructures on chain conformation, we simulated the chain sequence by assigning each monomer, namely $(R, R)\text{-8DL}^{\text{Me}}$, $(S, S)\text{-8DL}^{\text{Me}}$, and $(R, S)\text{-8DL}^{\text{Me}}$, an individual enrichment probability and then propagating for a total length of 50 repeating units. The sequence simulation on *sr*-P3HB $_{[52]}$ shows abundant continuous $[rr]$ segments existing in the polymer chain (Fig. 2F), which may

play a role in its viscoelastic properties and adhesion performance. Such continuous $[rr]$ segments rigidify polymer chains and serve as physical cross-linking points, leading to the formation of polymeric networks within the main body of the materials that can effectively dissipate external energy.

Stereomicrostructure-regulated adhesive properties

The adhesion performance of the obtained P3HB materials with diverse stereomicrostructures, spanning gradually from *it*- to *ir*-, *at*-, and then to *sr*- to *st*-tacticities, was systematically evaluated through lap-shear adhesion testing. During a lap-shear adhesion test, the exerted force, one of the most common forces a material faces at the bonded joint during service, is applied to the substrate in opposite directions to measure the ability of a material to withstand stress set in a plane. The adhesion strength is quantified from the maximum force at failure divided by the overlap area of the substrates. Chemically or physically treating substrates, such as with strong acid or through polishing or sandblasting (14, 33), are commonly used techniques for lap-shear tests to increase the surface roughness and thereby the contacting area between the adhesives and

the substrates. As this substrate pretreatment is not favored in daily applications, the substrates used in this study were untreated and simply cleaned with Kimwipes before adhesion, unless noted otherwise for comparative studies.

As shown in Fig. 3A, the adhesion strength of P3HB on aluminum substrates is largely determined by its stereomicrostructures, best represented here by percentages of $[rr]$ triads as its degree of (syndiotactic triad) stereoregularity. For example, both *it*- and *ir*-P3HB_[0] devoid of $[rr]$ triads did not display any adhesion behavior on aluminum substrates, regardless of variations in other triad values, $[mm]$ and $[mr]$ (table S4). In these cases, the specimens typically broke from the interface of the adhesive layer and the substrate while being mounted to the instrument for the lap-shear test. *at*-P3HB_[32] began to show adhesive behavior with a medium adhesion strength of 1.2 MPa, whereas *sr*-P3HB exhibited a wide range of adhesion strength from medium (1.9 MPa) to high (9.5 MPa) adhesion forces, depending on specific $[rr]$ values (Fig. 3A). With an increase in the stereoregularity of *sr*-P3HB from $[rr]$ of 42% to 84%, the adhesion strength first increased from 6.1 MPa (42% $[rr]$) to 9.5 MPa (52% $[rr]$) and then gradually decreased to

1.9 MPa (84% $[rr]$), demonstrating the effectiveness of stereomicrostructural engineering in regulating the adhesion performance of P3HB. When the stereoregularity was further improved to $[rr] = 88\%$ (*st*-P3HB_[88]), the P3HB became very brittle and did not bond the aluminum substrate. Notably, *ir*-P3HB_[0] and *sr*-P3HB_[52] exhibit similar thermal properties, such as T_g (11°C compared with 12°C) and T_m (109°C compared with 106°C), and both polymers are mechanically tough, with a good elongation at break (>350%) and ultimate tensile stress of ~23 MPa, yet they display drastically different adhesion behavior: ~0 MPa for *ir*-P3HB_[0] and 9.5 MPa for *sr*-P3HB_[52]. These comparative results affirm the essential role of the P3HB stereomicrostructures in adhesion properties. The superior adhesion performance of *sr*-P3HB could be attributed to its appropriate viscoelastic properties and the presence of abundant $[rr]$ blocks, where the rigid $[rr]$ blocks serve two roles: (i) as cross-linking points to create the network in the main body of the adhesives and (ii) improving polymer-substrate interactions, likely by leveraging multivalency.

We next shifted our attention to steel substrates. The adhesion strength of *sr*-P3HB

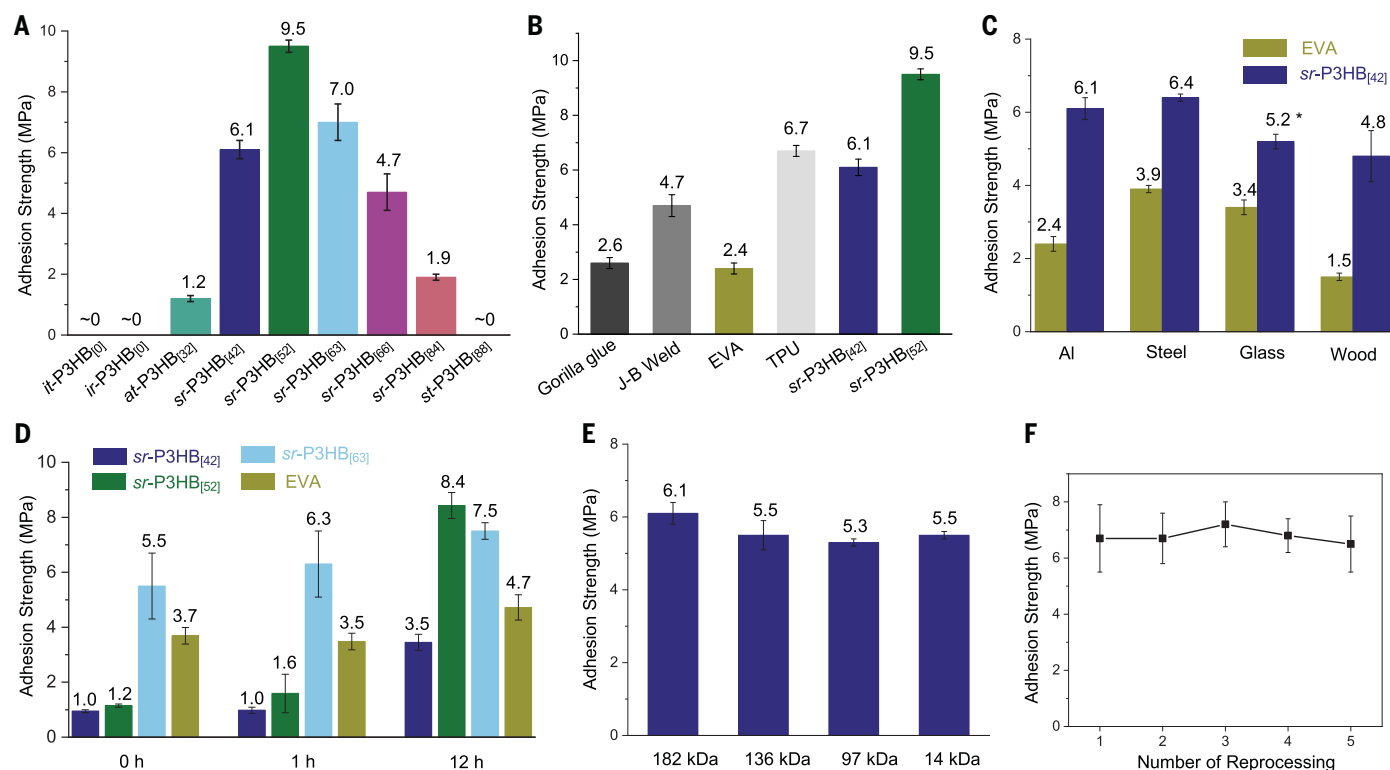


Fig. 3. Evaluation of adhesion strength of P3HB adhesives. (A) Adhesion strength of P3HB materials of various stereomicrostructures on aluminum substrate evaluated by lap-shear adhesion testing. (B) Adhesion strength of *sr*-P3HB and common commercial glues measured on an aluminum substrate. (C) Comparison of the adhesion strength of *sr*-P3HB_[42] and EVA hot melt measured on various substrates, including aluminum, steel, glass, and wood. Asterisk symbol indicates that glass

substrates broke before maximum force was reached. (D) Adhesion strength as a function of annealing time at ambient conditions for *sr*-P3HB_[42], *sr*-P3HB_[52], *sr*-P3HB_[63], and EVA hot melt (measured on steel substrates). (E) Adhesion strength of *sr*-P3HB_[42] as a function of molar mass (M_n) measured on aluminum substrates. (F) Adhesion strength of *sr*-P3HB_[42] as a function of the number of reprocessing on steel substrates. Error bars represent a standard derivation of five specimens.

exhibited a similar trend to that on aluminum substrates, with *sr*-P3HB_[42] (6.4 MPa) and *sr*-P3HB_[52] (10.7 MPa) performing the best (fig. S28A). As anticipated, compared with untreated substrates, sandblasted surfaces offered a much-enhanced adhesion strength on Al (~60% stronger adhesion, increased from 6.1 MPa to 9.8 MPa for *sr*-P3HB_[42]) and on steel substrates (~30% stronger adhesion; fig. S28B). Thus, P3HB adhesives, even when applied to untreated substrates, perform comparably to, or much better than, the state-of-the-art bioderived thermoset adhesives, such as the epoxidized soy oil-based adhesive with an adhesion of ~10 MPa on sandblasted Al after curing at 180°C for 6 hours (14) and the lignin-based adhesive with an adhesion strength of ~1.5 MPa on wood substrates after curing at 190°C for 8 min (15). Furthermore, the adhesion strength of *sr*-P3HB_[52,63] PHAs outperformed widely used commercial glues, represented here by Gorilla Glue and J-B Weld as well as EVA and thermoplastic polyurethane (TPU) hot melts, which were evaluated under identical conditions on aluminum substrates (Fig. 3B). Compared with the EVA hot melt, the glue we specifically target for replacement, *sr*-P3HB_[42] displayed substantially improved adhesion strength (by 64 to 220%) on various substrates (aluminum, steel, glass, and wood; Fig. 3C), indicating the potential of biodegradable P3HB adhesives to be a drop-in replacement for hot-melt EVA. Notably, the adhesion strength of *sr*-P3HB_[42] on glass was so strong that the substrates always broke before the adhesive joint failed (fig. S29A). Depending on the crystallization rate determined by the backbone stereoregularity, P3HB adhesives display largely tunable set and open times under ambient conditions (Fig. 3D). For *sr*-P3HB_[42,52], which have relatively lower stereoregularity and thus a slower crystallinity rate, a longer set time (>1 hour) is required for each to reach a serviceable adhesion strength of >3 MPa, whereas a practical adhesion force of 5.5 MPa was immediately achieved for *sr*-P3HB_[63] with a higher backbone stereoregularity, which rivals the set time of commercial EVA hot melt and is superior in terms of adhesion strength.

To evaluate the environmental stability of the P3HB adhesives, we first tested P3HB's suitability for an underwater pelletizing process envisioned for its large-scale production, using a setup to drop melt P3HB into water. We observed no change in its molar mass before or after this process, indicating its stability during this process. Second, we compared the adhesion strengths of *sr*-P3HB_[42] specimens prepared under different levels of relative humidity (RH) and days of ambient-condition storage (between the test and initial synthesis): 37% RH (indoor ambient), 1 day; 37% RH (indoor ambient), 1 year; and 77% RH (controlled humidity chamber), 1 year. These conditions resulted

in an adhesion strength of 3.5 ± 0.3 MPa (Fig. 3D), 3.4 ± 0.3 MPa (fig. S28C), and 3.5 ± 0.4 MPa (fig. S28C), respectively, therefore showing essentially constant performance under these different humidity levels and storage times. The degree of crystallinity also had a substantial impact on optical transparency of the P3HB adhesives, with the less crystalline one being more transparent, and both *sr*-P3HB_[42] and *sr*-P3HB_[52], with a moderate degree of crystallinity, exhibiting better transparency than that of EVA hot melt (fig. S29B).

To examine the molar mass effect on the adhesion strength, *sr*-P3HB_[42] materials with M_n ranging from 14 to 182 kDa were synthesized, and they all displayed similar adhesion forces of ~5.5 MPa (Fig. 3E), suggesting that the molar mass, within a reasonable range, has little to negligible impact on adhesion behavior. This independence of adhesion strength from molar mass is in stark contrast to the mechanical properties of polyesters (which are highly M_n sensitive) and will undoubtedly benefit at-scale production in terms of batch-to-batch variation and reprocessability. To test the reusability of the P3HB adhesive, lap-shear speci-

mens were repeatedly subjected to the adhesion test and rejoined upon melting after each failure. Owing to the thermoplastic nature and the adhesion insensitivity to the change in molar mass upon repeated heating and processing, *sr*-P3HB_[42] exhibited negligible changes in the adhesion strength even after the fifth reprocessing (Fig. 3F).

Alternatively, *ir*-, *at*-, and *sr*-P3HB PHAs produced from the ROP of BBL, which is readily accessible at industrially relevant scale, were also evaluated for their adhesion performance (fig. S30). Consistently, *ir*-P3HB_[7], with a low percentage of *[rr]* triads, lacked any adhesion behavior on aluminum substrates; *at*-P3HB_[24] displayed a limited adhesion strength of 0.14 MPa; and *sr*-P3HB_[61] showed the highest adhesion force (6.2 MPa), reinforcing the importance of stereomicrostructures, particularly *[rr]* triads, in regulating the adhesive behavior of P3HB.

Techno-economic analysis and life cycle assessment

To estimate the economic and environmental potential for P3HB adhesives, we performed techno-economic analysis (TEA) and life cycle

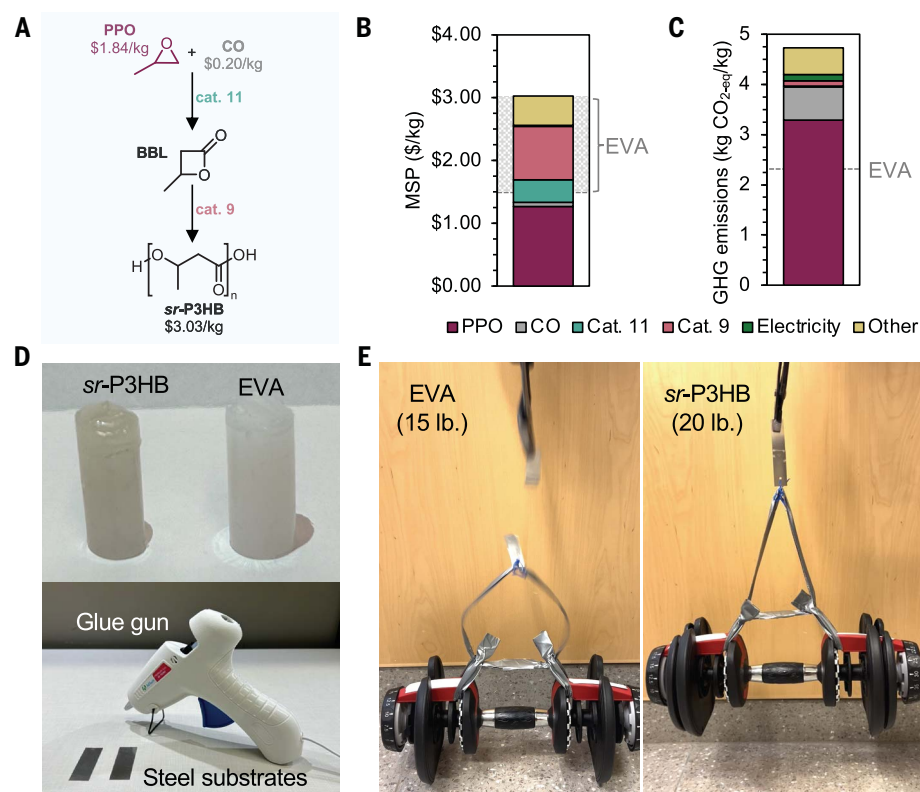


Fig. 4. TEA, LCA, and application demonstration of P3HB adhesives. (A) Diagram for the production of *sr*-P3HB from BBL and CO. (B) Minimum selling price and (C) GHG emissions for P3HB adhesive broken down by contribution. The gray EVA labels correspond to the price range from a combination of free online sources and market databases and the GHG emissions for EVA from the ecoinvent database. (D) The melt-processed P3HB glue stick and the application demonstration with a commercial glue gun. (E) The steel substrates glued together with EVA and *sr*-P3HB_[61] and tested to lift different weights, showing that EVA failed to lift 15 lb (~6.8 kg), but *sr*-P3HB lifted 20 lb (~9.1 kg) without breaking.

assessment (LCA) for *sr*-P3HB adhesive production from BBL (Fig. 4A) that produces *sr*-P3HB_[61] with an adhesion strength of 2.5× that for EVA. BBL is produced onsite through the catalytic carbonylation of purchased propylene oxide (PPO) and then polymerized without added solvent using an yttrium-based catalyst (fig. S1, 9). A base case was established assuming fossil-derived PPO (\$1840/tonne) and CO (\$195/tonne) feedstocks. The minimum selling price (MSP, all costs in 2020\$) was \$3.03/kg P3HB, which is slightly higher than the 2022 selling price of \$2.26/kg for EVA (34) (Fig. 4B). PPO and CO raw materials contribute \$1.34/kg_{P3HB} to the MSP. The carbonylation and polymerization catalysts contribute \$0.36/kg_{P3HB} and \$0.85/kg_{P3HB}, respectively, driven largely by their high estimated prices (catalyst 11: \$331/kg; catalyst 9: \$241/kg). Despite the potential for near-term cost competitiveness, LCA revealed that the P3HB adhesive exhibited higher impacts compared with EVA across all categories (fig. S33). Greenhouse gas (GHG) emissions were 4.73 kg CO₂-eq/kg_{P3HB} (Fig. 4C), which is approximately double the emissions associated with EVA production (2.35 kg CO₂-eq/kg). Results were dominated by the PPO and CO feedstocks, which together accounted for between 54 and 96% of impacts across all categories. Utilization of biobased rather than conventional fossil-derived feedstocks (PPO from wood-based methanol and CO from high-temperature electrolysis) led to a slight decrease in GHG emissions (4.09 kg CO₂-eq/kg) yet increased the MSP substantially, to \$4.31/kg_{P3HB}, because of higher feedstock costs (see supplementary materials for additional details on the biobased route). As the P3HB adhesives were shown to be highly reprocessible (Fig. 3F), this could enable opportunities for direct reuse that are not possible with traditional thermoset adhesives. Nonetheless, new routes to the chemical precursors (BBL or 8DL^{Me}) will be needed to substantially reduce environmental impacts of the primary production. Conceptually, the direct reprocessing of the P3HB adhesive would require minimal heating relative to its production and would result in a linear decrease in process costs and impacts (35).

Real-world demonstrations of P3HB adhesives

An important part of creating biodegradable replacements for traditional nondegradable products is that they can perform similarly to, or better than, the incumbents. To evaluate the biodegradable P3HB adhesive in this study, we devised several experiments to test its properties in real world applications. Owing to the suitable crystallinity and crystallization rate, *sr*-P3HB_[61] could be readily molded into a glue stick that resembles a typical EVA glue stick (Fig. 4D). This P3HB glue stick could be used as a drop-in replacement in a commercially available glue gun. To show this drop-in replacement

in action, we visualized the strength of the P3HB adhesive in comparison to EVA on steel substrates. We extruded EVA and *sr*-P3HB_[61] from the same model of glue gun, onto steel substrates and allowed for the same set time and adhesion area. Then the substrates were used to lift various amounts of weight (Fig. 4E). EVA broke when lifting 15 lb (~6.8 kg), whereas *sr*-P3HB_[61] was able to lift to 20 lb (~9.1 kg), demonstrating that the P3HB replacement outperforms typical hot-melt adhesives (movie S1). We also showed the P3HB adhesives can be used in packaging by sealing a shipping-ready cardboard box (movie S2 and fig. S36). A strong bond was created between the cardboard box and *sr*-P3HB_[61], allowing 9.8 lb (~4.4 kg) of book to be lifted, and *sr*-P3HB_[61] was easily applied with a glue gun.

The ability to access the entire range of synthetically engineered stereomicrostructures has enabled elucidation of the fundamental relationship between the stereomicrostructure and adhesion property of P3HB. In turn, this study has led to the discovery that *sr*-P3HB with continuous rigid [77] sequence segments exhibits higher adhesion strength than common commercial adhesives and can also be fine-tuned by varying the relative stereoregularity for tailored adhesion strength. In stark contrast, other tacticities show negligible or nonmeasurable adhesion. Our combined experimental and simulation studies indicate that the stereoregularity-dependent adhesion property of P3HB originates from its viscoelastic properties and chain configurations and conformations, which are dictated by the stereomicrostructures determining not only the general tacticity but also the overall stereoregularity in the context of stereo-sequences of the chiral centers. The TEA and LCA evaluations of the economic and environmental impacts of P3HB adhesives production show that the P3HB adhesives can be cost-competitive with the petroleum-based nonrecyclable or non-biodegradable incumbent adhesives and reveal the main cost and environmental impact drivers for needed further developments of more efficient monomer, catalyst, and polymer synthesis and production at scale. Overall, *sr*-P3HB adhesives exhibit tunable adhesion strength and are biodegradable and recyclable through repeated melt-reprocessing cycles with constant adhesion performance and thus offer a more sustainable alternative to the incumbent adhesives.

REFERENCES AND NOTES

1. E. M. Petrie, *Handbook of Adhesives and Sealants* (McGraw-Hill, ed. 2, 2007).
2. Adhesives and Sealants Market Size and Forecasts 2020-2030, The Insight Partners, Report No. 5892948; <https://www.researchandmarkets.com/reports/5892948/adhesives-sealants-market-size-forecasts#cat-pos-1> [accessed 14 May 2024].
3. L. D. Ellis et al., *Nat. Catal.* **4**, 539–556 (2021).
4. S. B. Borrelle et al., *Science* **369**, 1515–1518 (2020).
5. R. Geyer, J. R. Jambeck, K. L. Law, *Sci. Adv.* **3**, e1700782 (2017).

6. World Economic Forum, Ellen MacArthur Foundation and McKinsey & Company, "The new plastics economy: Rethinking the future of plastics" (2016); <https://www.ellenmacarthurfoundation.org/the-new-plastics-economy-rethinking-the-future-of-plastics>.
7. F. Vidal et al., *Nature* **626**, 45–57 (2024).
8. C. Shi, E. C. Quinn, W. T. Diment, E. Y.-X. Chen, *Chem. Rev.* **124**, 4393–4478 (2024).
9. G. W. Coates, Y. D. Getzler, *Nat. Rev. Mater.* **5**, 501–516 (2020).
10. M. Hong, E. Y.-X. Chen, *Green Chem.* **19**, 3692–3706 (2017).
11. A. V. Pocius, *Adhesion and Adhesives Technology: An Introduction* (Carl Hanser Verlag GmbH & Co. KG, 2021).
12. S. Pal et al., *Science* **385**, 877–883 (2024).
13. L. A. Heinrich, *Green Chem.* **21**, 1866–1888 (2019).
14. C. R. Westerman, B. C. McGill, J. J. Wilker, *Nature* **621**, 306–311 (2023).
15. G. Yang, Z. Gong, X. Luo, L. Chen, L. Shuai, *Nature* **621**, 511–515 (2023).
16. N. Jarach, H. Dodiuk, in *Biobased Adhesives: Sources, Characteristics and Applications*, M. Dunky, K. L. Mittal, Eds. (Wiley, 2023), pp. 427–461.
17. J. R. Pereira et al., *Int. J. Biol. Macromol.* **122**, 1144–1151 (2019).
18. M. Viljanmaa, A. Södergård, P. Tormala, *Int. J. Adhes. Adhes.* **22**, 219–226 (2002).
19. T. Narancic et al., *Environ. Sci. Technol.* **52**, 10441–10452 (2018).
20. A. H. Westlie, E. C. Quinn, C. R. Parker, E. Y.-X. Chen, *Prog. Polym. Sci.* **134**, 101608 (2022).
21. Z. A. Raza, S. Abid, I. M. Banat, *Int. Biodeterior. Biodegradation* **126**, 45–56 (2018).
22. G.-Q. Chen, *Chem. Soc. Rev.* **38**, 2434–2446 (2009).
23. K. Sudesh, H. Abe, Y. Doi, *Prog. Polym. Sci.* **25**, 1503–1555 (2000).
24. H. M. Müller, D. Seebach, *Angew. Chem. Int. Ed.* **32**, 477–502 (1993).
25. Z. Zhang et al., *Angew. Chem. Int. Ed.* **62**, e202311264 (2023).
26. E. C. Quinn et al., *J. Am. Chem. Soc.* **145**, 5795–5802 (2023).
27. X. Tang, A. H. Westlie, E. M. Watson, E. Y.-X. Chen, *Science* **366**, 754–758 (2019).
28. X. Tang, E. Y.-X. Chen, *Nat. Commun.* **9**, 2345 (2018).
29. M. G. Mazzotta, A. A. Putnam, M. A. North, J. J. Wilker, *J. Am. Chem. Soc.* **142**, 4762–4768 (2020).
30. F. Awaja, M. Gilbert, G. Kelly, B. Fox, P. J. Pigram, *Prog. Polym. Sci.* **34**, 948–968 (2009).
31. E. Perret, F. A. Reiffer, A. Gooneie, R. Hufenus, *Polymer* **180**, 121668 (2019).
32. M. Yokouchi, Y. Chatani, H. Tadokoro, K. Teranishi, H. Tani, *Polymer* **14**, 267–272 (1973).
33. M. A. Rahman et al., *Sci. Adv.* **7**, eabk2451 (2021).
34. Business Analytiq, Ethylene vinyl acetate (EVA) price index; <https://businessanalytiq.com/procurementanalytics/index/ethylene-vinyl-acetate-eva-price-index/> [accessed 3 December 2024].
35. S. R. Nicholson et al., *Annu. Rev. Chem. Biomol. Eng.* **13**, 301–324 (2022).

ACKNOWLEDGMENTS

We thank R. Gowda and R. Li for preparation of the catalysts used in BBL polymerization and E. Rettner and C. Dojan for the creation of a glue-stick mold. **Funding:** Z.Z., E.C.Q., J.K.K., J.S.D., L.Z., G.T.B., and E.Y.-X.C. acknowledge funding support by the US Department of Energy, Office of Energy Efficiency and Renewable Energy, Advanced Materials and Manufacturing Technologies Office (AMMTO) and Bioenergy Technologies Office (BETO). This work was performed as part of the BOTTLE (Bio-Optimized Technologies to Keep Thermoplastics out of Landfills and the Environment) Consortium and funded under contract no. DE-AC36-08G028308 with the National Renewable Energy Laboratory, operated by Alliance for Sustainable Energy. The BOTTLE Consortium includes members from Colorado State University, T.X., A.G., and T.C. acknowledge funding support by the US Department of Energy, Office of Science, Office of Basic Energy Sciences, Materials Sciences and Engineering Division under contract no. DE-AC02-05CH11231 (Organic-Inorganic Nanocomposites KC3104). This research used resources of the National Synchrotron Light Source II, a US Department of Energy (DOE) Office of Science User Facility operated for the DOE Office of Science by Brookhaven National Laboratory under contract no. DE-SC0012704. A.G. acknowledges funding support by the National Science Foundation Graduate Research Fellowship under grant no. DGE-2146752. **Author contributions:** Conceptualization: E.Y.-X.C. Methodology: Z.Z. and E.C.Q. Investigation: Z.Z., E.C.Q., and L.Z. TEA and LCA: J.K.K., J.S.D., and G.T.B. Sequence simulation, SAXS/WAXS, rheology: A.G., T.C., and T.X. Funding acquisition: G.T.B., T.X., and E.Y.-X.C. Writing – original draft: Z.Z. and E.C.Q. Writing – review & editing: All authors. **Competing interests:** E.Y.-X.C., Z.Z., and E.C.Q. are named inventors on a pending US

patent application (18/492,554), which is based on provisional applications 63/524,397 (30 June 2023) and 63/418,109 (21 October 2022), submitted by the Colorado State University Research Foundation, which covers PHA adhesives. The other authors declare that they have no competing interests. **Data and materials availability:** All data are available in the main text or the supplementary materials. **License information:** Copyright © 2025 the authors, some rights reserved; exclusive licensee American

Association for the Advancement of Science. No claim to original US government works. <https://www.science.org/about/science-licenses-journal-article-reuse>

SUPPLEMENTARY MATERIALS

science.org/doi/10.1126/science.adr7175
Materials and Methods

Figs. S1 to S45
Tables S1 to S5
References (36–65)
Movies S1 and S2

Submitted 14 July 2024; accepted 10 December 2024
[10.1126/science.adr7175](https://doi.org/10.1126/science.adr7175)